

Measurement of the critical intensity in a LAr calorimeter module of the Hilum experiment

Bachelor-Arbeit
zur Erlangung des Hochschulgrades
Bachelor of Science
im Bachelor-Studiengang Physik

vorgelegt von

Fabian Petsch
geboren am 23.05.1994 in Belzig

Institut für Kern- und Teilchenphysik
Fachrichtung Physik
Fakultät Mathematik und Naturwissenschaften
Technische Universität Dresden
2016

Eingereicht am 09. September 2016

1. Gutachter: Prof. Dr. Arno Straessner
2. Gutachter: Prof. Dr. Michael Kobel

Summary

Abstract

English:

The Hilum (high luminosity) experiment at the Institute of High Energy Physics (IHEP) in Protvino (Russia) provides valuable information on the behaviour of the liquid argon (LAr) calorimeter components of ATLAS under the conditions expected at the high luminosity LHC stage. Data obtained from a Hilum electromagnetic end-cap module (EMEC) allows for a thorough investigation of the detectors properties. In particular, the critical intensity that distinguishes the linear and non-linear operating regimes of the calorimeter shall be determined. Systematic uncertainties due to the different data taking periods need to be discussed and included in the existing data. A chi-squared fit is employed in order to estimate the missing systematics. Finally, the outcome of the fit is to be tested with regard to its stability and validity.

Abstract

Deutsch:

Das Hilum-Experiment am Institut für Hochenergiephysik (IHEP) in Protvino (Russland) erlaubt es, das Verhalten der Flüssig-Argon-Komponenten des Kalorimeter-Systems von ATLAS unter den Bedingungen, die für die High-Luminosity-LHC-Phase erwartet werden, zu testen. Mithilfe von Messungen am elektromagnetischen Endkappen-Modul von Hilum können die Eigenschaften des Detektors und der Auslese-Elektronik untersucht werden. Insbesondere soll dabei die kritische Strahlintensität bestimmt werden, die den Übergang vom linearen zum nicht-linearen Messbereich des Kalorimeters kennzeichnet. Um dies zu tun, müssen gegebenenfalls bisher unberücksichtigte systematische Unsicherheiten diskutiert und den bestehenden Daten hinzugefügt werden. Ein Chi-Quadrat-Fit wird genutzt, um die fehlenden Systematiken abzuschätzen. Abschließend wird die Güte (Stabilität und Aussagekraft) des Fits geprüft.

Contents

Introduction	7
The Hilum experiment	11
2.1 The U-70 accelerator	11
2.2 Hilum set-up	11
2.3 The EMEC module	12
The Hilum data	13
3.1 EMEC data sample	13
3.1.1 Full data set with unmodified uncertainties	13
3.1.2 Properties of the data set	13
3.2 HV current measurement	16
3.2.1 HV current signal	16
3.2.2 HV uncertainties	17
3.3 Expected HV current behaviour	17
3.3.1 Space charges and electric field of LAr gaps	17
3.3.2 HV current model	18
Chi-squared fit	21
4.1 Theory on Chi-squared test	21
4.2 Estimating the unknown systematics	21
4.2.1 HV current for very low intensities	22
4.2.2 Linear fits within low intensity range	22
4.2.3 HV current binning	23
4.3 Fit results	25
4.4 Fit stability	28
Summary and Outlook	31
Appendix	33
A.1 Average HV current per data taking period	33
A.2 List of data taking periods	34
A.3 Widths of HV current bins.	35

A.4	Estimating the uncertainty intervals for multi-parameter chi-squared fits . . .	35
A.5	Theory on correlation	36
A.6	Hilum data correlation	37
	Bibliography	39

Introduction

The Large Hadron Collider (LHC) [1] at CERN¹ is the largest particle accelerator that has been built to date. It is currently operating at a center-of-mass energy of 13 TeV and just recently achieved its design luminosity² of $1 \cdot 10^{34} \text{ cm}^{-2} \text{ s}^{-1}$. The LHC is about to undergo major upgrade work between 2018 and 2025 [2]. The main purpose is to reach a luminosity of up to $7 \cdot 10^{34} \text{ cm}^{-2} \text{ s}^{-1}$. In addition to the accelerator itself, its experiments also have various upgrade plans in order to cope with the new scenario, e.g. the higher detector occupancies. This includes ATLAS³ [3], which is the largest detector of the LHC [4] [5].

ATLAS is a general-purpose experiment designed to measure pp and AA collisions⁴. It consists of multiple layers each specifically designed to serve a distinct purpose whilst searching for different types of particles. Essentially, the detector is made up of three constituents: The inner tracking detector, the calorimeter and the muon spectrometer.

The calorimeter system measures the deposited energy of the particles. It consists of the Tile Calorimeter (TileCal) and the Liquid Argon (LAr) calorimeter. The latter includes the electromagnetic barrel calorimeter, the electromagnetic end-cap calorimeter (EMEC), the hadronic endcap calorimeter (HEC) and the forward calorimeter (FCal) (see Fig. 1.1).

The EMEC (see Fig. 1.2) covers a pseudorapidity⁵ range of $1.375 < |\eta| < 3.2$ [6] and its electrodes are supplied with a high voltage (HV). The HV current depends on the particle flux that reaches the EMEC, as for higher beam intensities more and more argon atoms become ionized. Unfortunately, towards higher luminosity values, the dependency becomes non-linear due to the build-up of space-charge regions of ionized plasma shielding the electrodes. This effect is of particular importance when it comes to the HL-LHC phase⁶.

The U-70 proton synchrotron at IHEP⁷ in Protvino (Russia) has been used to obtain testbeams for the ATLAS endcap calorimeter subsystems (eg. in [7]). This thesis aims to investigate the relation between the HV current and the beam intensity for the EMEC test module in Protvino. In particular, the critical intensity marking the detector's behaviour transitioning from linear to non-linear shall be determined.

¹Conseil Européen pour la Recherche Nucléaire (European Organization for Nuclear Research)

²number of collisions per time and cross section

³A Toroidal LHC Apparatus

⁴proton-proton and nucleus-nucleus

⁵a coordinate that describes the angle θ relative to the beam axis; $\eta = 0$ corresponds to $\theta = 90^\circ$ and $\eta = \infty$ to $\theta = 0$

⁶high luminosity LHC phase

⁷Institute for High Energy Physics

In sections 2.1 through 2.3 a description of the Hilum experiment and its EMEC module is given. Section 3.1 introduces the data set. The measurement methods for the HV current and the existing uncertainties are explained in section 3.2. The model that was used to fit the EMEC data is defined in section 3.3, which also gives a short justification with regard to the physics of LAr gaps. In section 4.2 the χ^2 fit is performed, where a brief introduction to χ^2 -fitting can be drawn from section 4.1. The final results are presented in section 4.3 and tested in section 4.4.

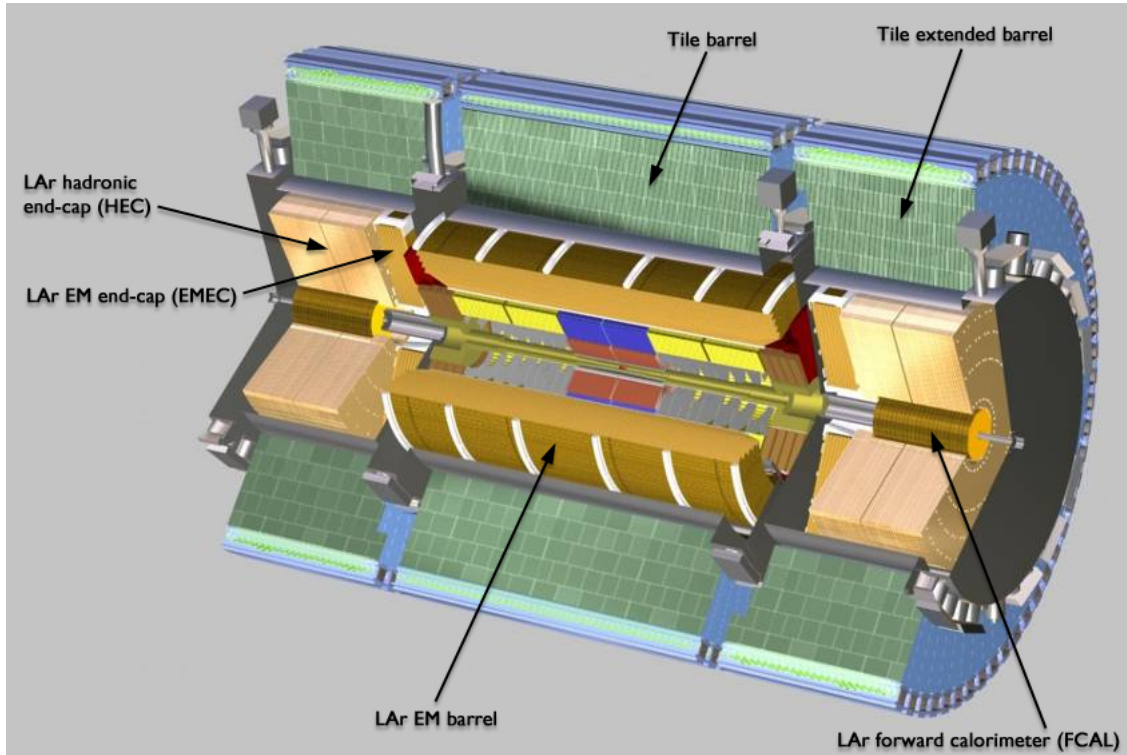


Figure 1.1: Calorimeter system of the ATLAS experiment [8].



Figure 1.2: A technician for the ATLAS collaboration, Michel Mathieu, cabling the electromagnetic end-cap [9].

The Hilum experiment

2.1 The U-70 accelerator

The U-70 accelerator at the Institute of High Energy Physics (IHEP) in Protvino currently is the sole proton synchrotron available for fixed-target research in Russia [10]. It operates at a maximum beam energy of 76 GeV and was built in 1967 [7].

The protons are provided in a bunched structure with a total of 30 bunch spots and a spacing of 165 ns [11]. For Hilum, only every 6th bunch is filled, thus leading to a spacing of approximately 1 μ s. Moreover, the beam energy only amounts to 50 GeV. One accelerator fill is extracted over a time period of circa 1.2s as a single spill [12]. The beam is obtained via a bent crystal technique.

The U-70 recently received an upgrade that allows for intensities up to 10^{12} p/s⁸ to be handled correctly. Since 10^9 p/s are roughly equivalent to the current luminosity of the LHC of $1 \cdot 10^{34}$ cm⁻² s⁻¹, Hilum data taking goes well beyond the intensities expected at the HL-LHC stage.

2.2 Hilum set-up

The set-up [13] of the experiment is shown in Fig. 2.1. The proton beam enters the set-up on the right-hand side. Its position is monitored by a secondary emission chamber (SEC) and a hodoscope (H), a matrix-like arrangement of 32 scintillation counters. The beam intensity is measured using the ionisation chamber (IC), the cherenkov counter (CH), aluminium foil (Al) and the scintillation counter monitor (SM). Furthermore, six scintillation counters are placed either directly into (S1, S2, S3) or alongside the beam-line (S4-S6, not depicted in Fig. 2.1). The latter detect any particles coming off the Fe absorbers once a proton has been scattered. Three cryostats, each enclosing an endcap module (i.e. HEC, EMEC and FCAL) are targeted by the proton beam. Blocks of multiple iron plates ensure that the conditions met in the cryostats match those found in the real ATLAS experiment.

A recent upgrade introduced another secondary emission chamber (SEC2) to allow more accurate beam positioning for high intensities.

⁸protons per spill

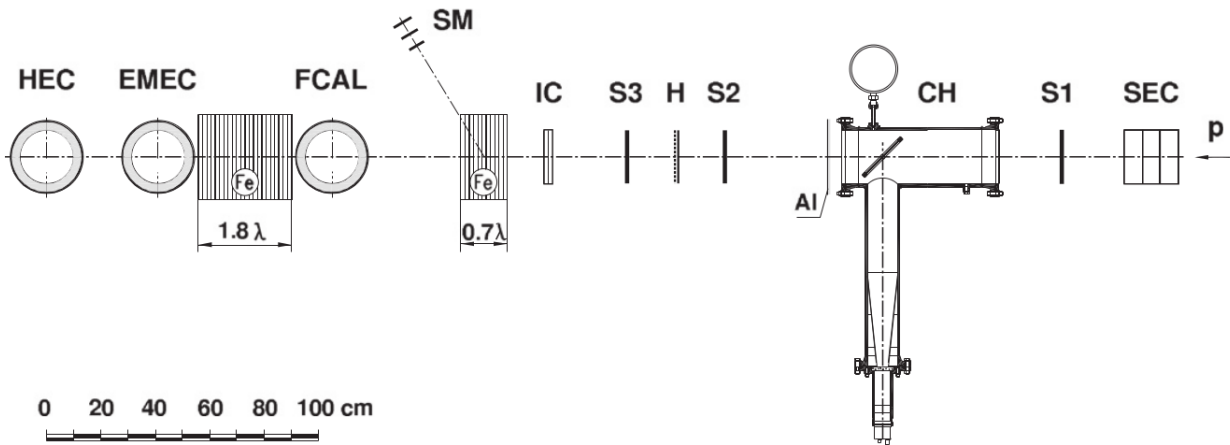


Figure 2.1: Hilum set-up [13].

2.3 The EMEC module

Fig. 2.2 illustrates the structure of the EMEC module. The beam entering from the right-hand side passes through four lead and stainless steel absorber sheets. In between three copper-plated Kapton electrodes are mounted. Each of those has a total sensitive area of $60\text{ mm}^2 \cdot 60\text{ mm}^2$ and is divided into four square pads. The LAr gap between the electrodes and the absorbers has a width of 2 mm.

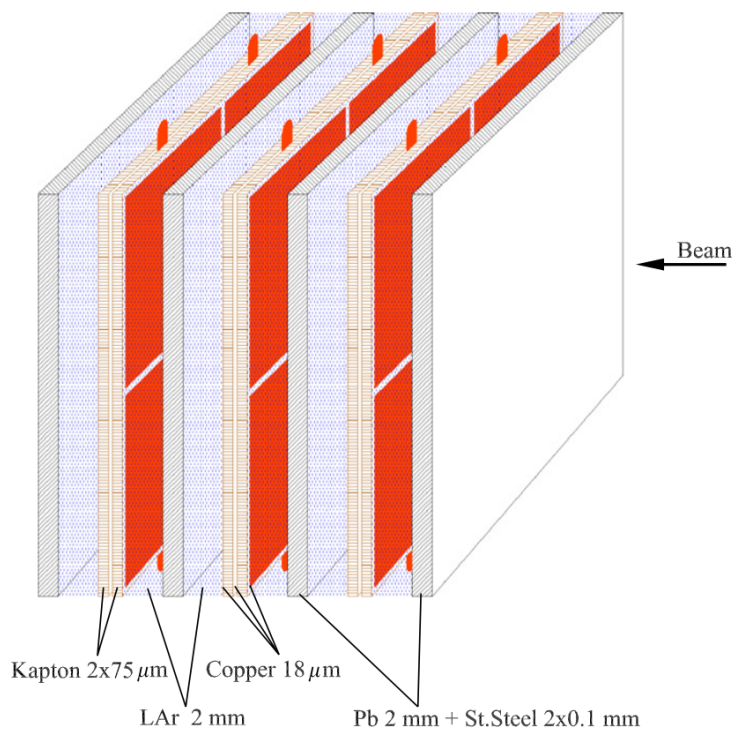


Figure 2.2: EMEC module [13]

The Hilum data

3.1 EMEC data sample

3.1.1 Full data set with unmodified uncertainties

The full data set, a total of 1231 data points, is depicted in Fig. 3.1. It is segmented into 33 data taking periods, called runs. For each run, the measurements were taken within a small intensity interval (compared to the full intensity range)⁹. The term 'raw' refers to the original data set without any modifications concerning the uncertainties.

For every run included in Fig. 3.1 the HV current has been measured using the amplitude method. Both the measuring methods of the HV current and its uncertainties are explained in 3.2.1 and 3.2.2 respectively. The HV current uncertainty bars cannot be seen in Fig. 3.1 due to their small size. The beam intensity uncertainty was set to 2.5% throughout [14].

3.1.2 Properties of the data set

Most runs are quite different from each other, e.g. with respect to the amount of data points, the relative spread and their correlation. The data set includes runs with only very few points (Fig. 3.2), several linear-shaped ones (Fig. 3.3) and point clusters (Fig. 3.4).

Furthermore, note that 385 data points lie below an intensity of $0.01 \cdot 10^9$ p/s and more than half the total amount, 657 to be precise, below a threshold of $1 \cdot 10^9$ p/s, which is not obvious from Fig. 3.1.

The uncertainties of the HV current do not cover the fluctuations of the measurement very well. For instance within the mid-range of the beam intensity, i.e. $50 \cdot 10^9$ p/s to $100 \cdot 10^9$ p/s, there seem to be large systematic shifts between the individual runs. The data cluster at about $1200 \mu\text{A}$ is taken from a single run (number 1165). In this instance, one would expect the uncertainty bars to overlap between the runs if they covered the systematics correctly.

There are several possible reasons for the large fluctuations: On the one hand, the beam position might have altered between the data taking periods. This would have led to unwanted loss or gain of beam intensity and account for the shifts observed from one run to another. Furthermore, there might have been beam movement during any of the individual runs, thus

⁹see appendix A.1 for a diagram showing the averaged HV current and beam intensity for each run and appendix A.2 for a full run list with corresponding correlation coefficients

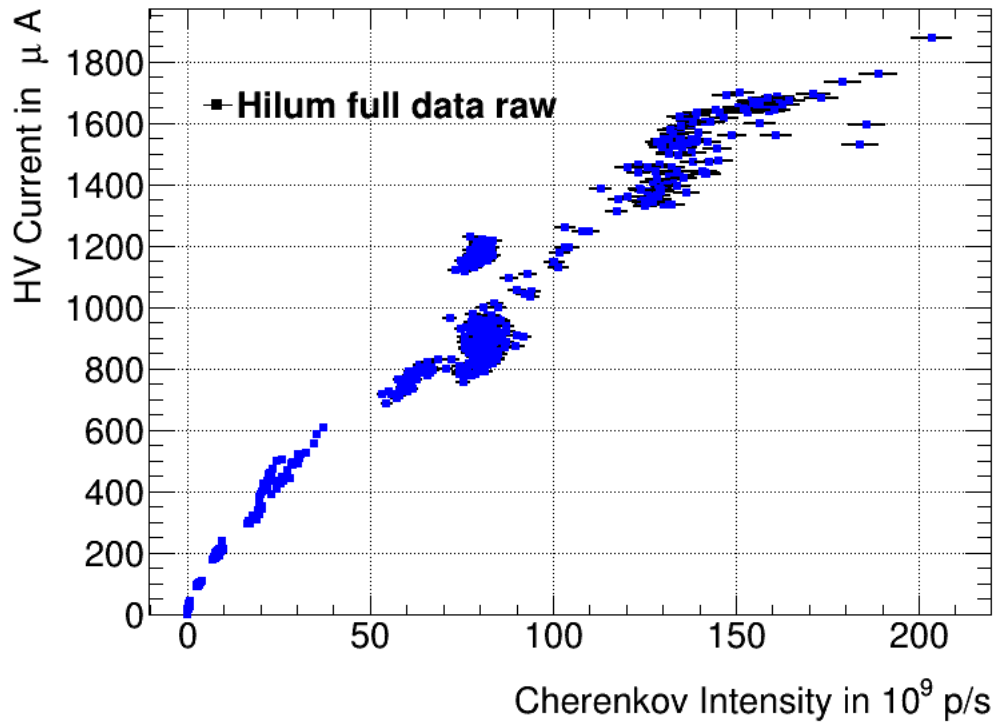


Figure 3.1: Hilum raw data.

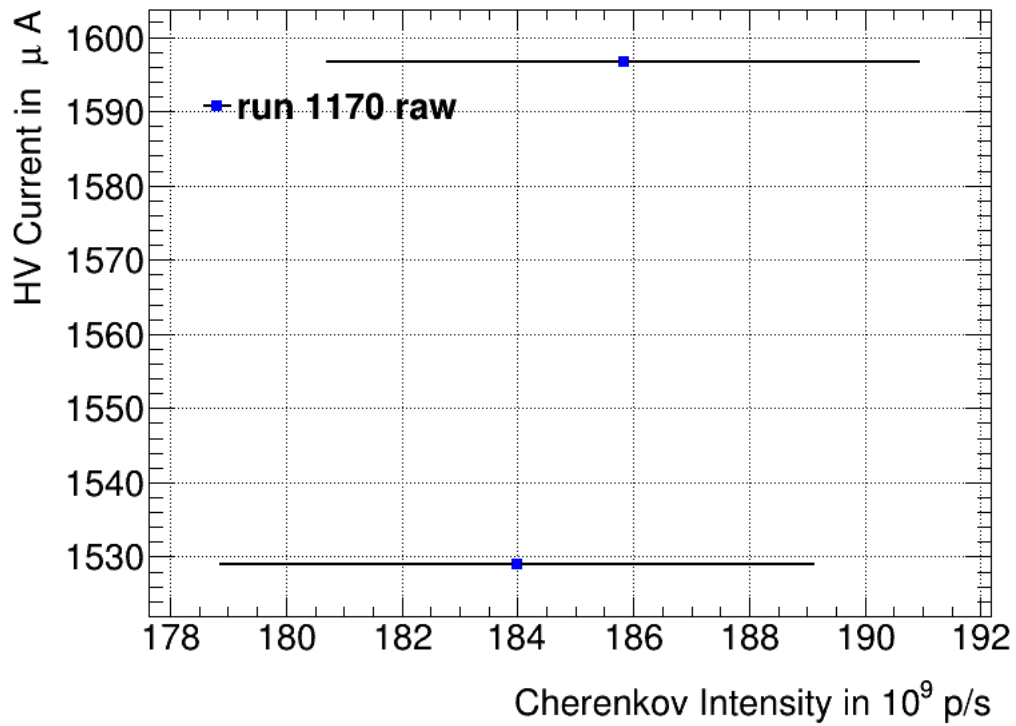


Figure 3.2: Run 1170 raw data.

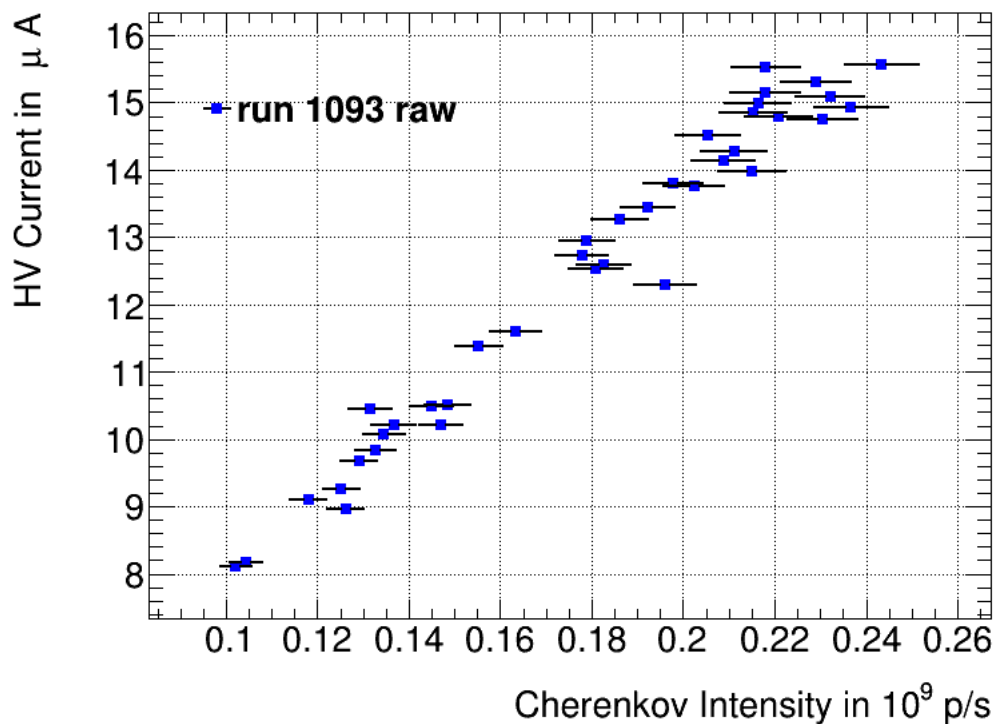


Figure 3.3: Run 1093 raw data.

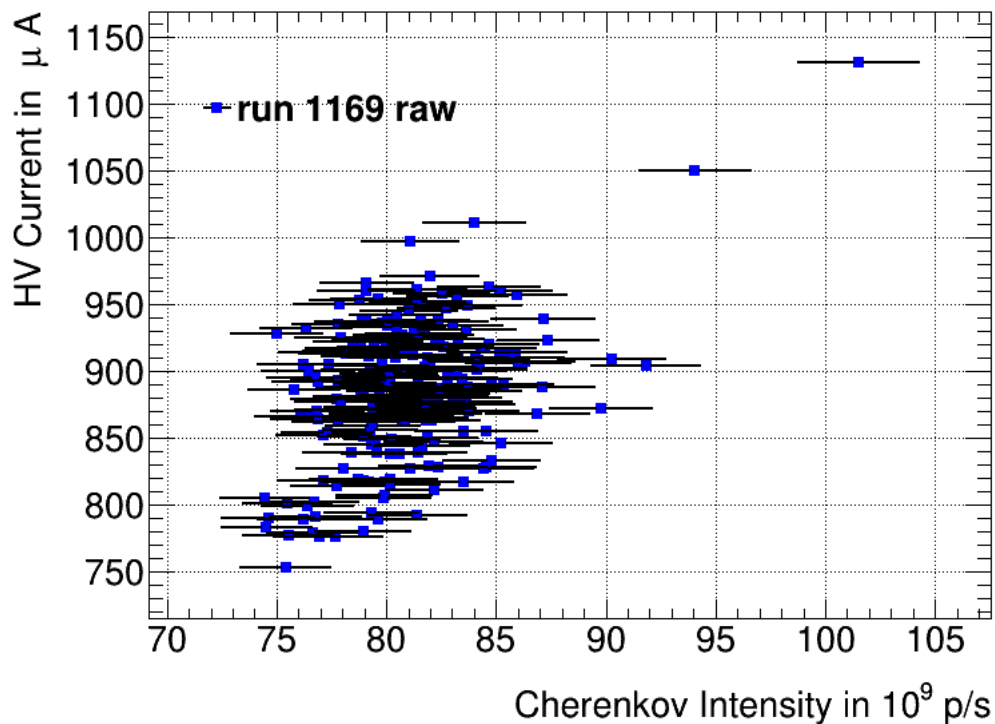


Figure 3.4: Run 1169 raw data.

giving a possible explanation for cluster-like data as seen in Fig. 3.4. On the other hand, a wrong calibration of the beam intensity could be a potential error source.

3.2 HV current measurement

3.2.1 HV current signal

The EMEC data sample was obtained via two different methods for measuring the HV current, the amplitude and the integral method.

The former determined the HV current by subtracting the baseline of the pulse from its maximum value (see Fig. 3.5). This produced some bias due to always getting the noise from the background. Especially for low amplitudes both the HV current and the noise were in the same order of magnitude. In this case the noise was likely to be picked up as the maximum value. To overcome this issue, it was decided to take the maximum of the sum of two or three data samples. Then the noise usually cancelled.

The integral method calculated the HV current by evaluating the integral of the pulse. Dividing its value by the length of the spill gave the mean value of the HV current.

Both methods thus differ in how they approximate the signal. The amplitude method overestimates it, as the HV current is assumed to be the maximum signal value for the entire peak, whereas the integral method provides a more moderate approach.

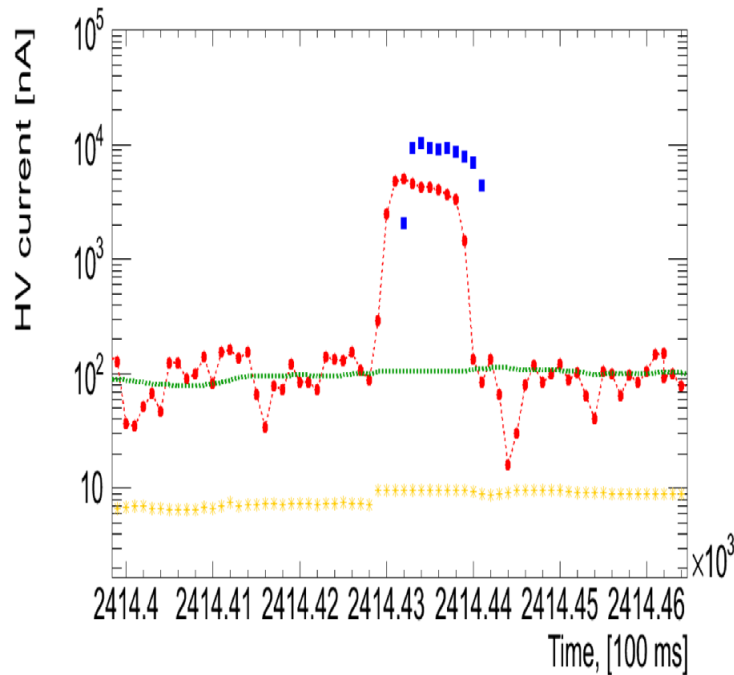


Figure 3.5: Shape of a single HV current pulse - the red dots represent the peak and baseline of the HV current [12].

3.2.2 HV uncertainties

The existing HV current uncertainties (see section 3.1.1) originate from the noise of the electronics.

For the amplitude method and considering just one sample the HV current I_{HV} is calculated as

$$I_{\text{HV}} = I_{\text{HV}}^{\text{max}} - I_{\text{B}}, \quad (3.1)$$

where I_{B} denotes the mean value of the baseline and $I_{\text{HV}}^{\text{max}}$ the maximum HV current value. Hence its corresponding uncertainty ΔI_{HV} with propagated uncertainties $\Delta I_{\text{HV}}^{\text{max}}$ and ΔI_{B} is

$$\Delta I_{\text{HV}} = \sqrt{(\Delta I_{\text{HV}}^{\text{max}})^2 + (\Delta I_{\text{B}})^2}. \quad (3.2)$$

The fluctuation of the pedestal ΔI_{B} is given by the standard error on its mean:

$$\Delta I_{\text{B}} = \sqrt{\frac{1}{m(m-1)} \sum_{i=1}^m (I_{\text{B}} - I_{\text{B},i})^2}, \quad (3.3)$$

with m representing the number of points used for the baseline calculation. Since the uncertainty of the maximum HV current value $\Delta I_{\text{HV}}^{\text{max}}$ is taken as the standard deviation of the baseline,

$$\Delta I_{\text{HV}}^{\text{max}} = \sqrt{m} \cdot \Delta I_{\text{B}}, \quad (3.4)$$

eq. 3.2 can be written as

$$\Delta I_{\text{HV}} = \Delta I_{\text{B}} \sqrt{1 + m}. \quad (3.5)$$

Error calculation for the integral method is omitted, because in the following only amplitude runs have been analysed.

3.3 Expected HV current behaviour

3.3.1 Space charges and electric field of LAr gaps

A LAr gap in the ATLAS calorimeter or the EMEC module in Hilum is presented by Fig. 3.6 as a schematic drawing. The left plate at $z = 0$ is supplied with a positive high voltage V_0 , whereas the right plate ($z = a$) is at ground. Electrons move to the anode and positively charged argon atoms to the cathode.

The argon ions possess a much smaller drift velocity than the electrons. For the LAr gaps in the EMEC module at a HV of 1.8 kV this leads to typical drift times of 20 ms for the positively

charged ions and 400 ns for the electrons [13]. When increasing the beam intensity, more argon atoms get ionized. For large intensities the charges are not collected fast enough by the electrodes. This leads to a build-up of positive ions.

For very low beam intensities a constant electric field is expected. However, for higher beam intensities it gets distorted (see Fig. 3.7). At about 10^9 p/s a field-free region with a size of 0.6 mm adjacent to the anode has developed. This reduces the effective gap size to about 1.4 mm.

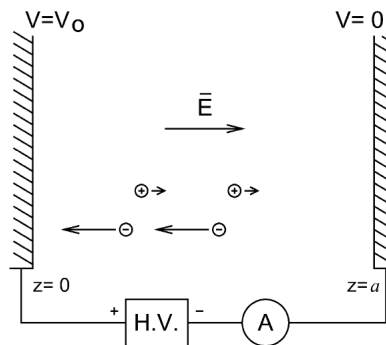


Figure 3.6: Schematic diagram of a LAr gap [15].

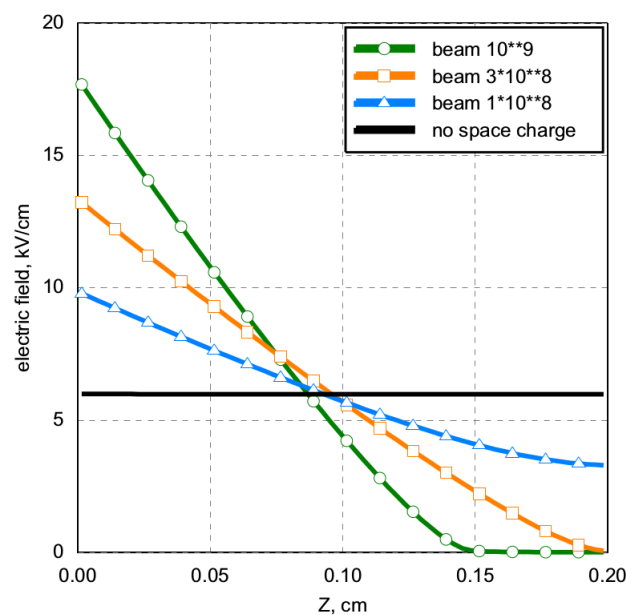


Figure 3.7: Simulated electric field for a gap size of 2.0 mm and a HV of 1.2 kV [13]. The anode is on the right-hand side.

3.3.2 HV current model

The data sample in Fig. 3.1 is expected to be represented by a piecewise defined fit function with four parameters[12]: It starts off with a linear part with offset I_0 and slope m for beam

intensities below the critical intensity I_{crit} . In this regime the HV current is directly proportional to the incoming particle flux. For values above I_{crit} , space-charge effects discussed in section 3.3.1 set in and a non-linear behaviour occurs. This is modelled by a power function with exponent p . Its value is expected to be ca. 0.75 [15]. The fit function then is as follows:

$$I_{\text{HV}} = I_0 + \begin{cases} m \cdot I & I < I_{\text{crit}} \\ m \cdot \frac{I^p}{I_{\text{crit}}^{p-1}} & I \geq I_{\text{crit}} \end{cases} . \quad (3.6)$$

In principal, the fit function will look as shown in Fig. 3.8, with an arbitrarily chosen parameter set of $I_0 = 0$, $m = 70 \mu\text{A}$ per 10^9 p/s and $p = 0.75$. I_{crit} is set to $20 \cdot 10^9$ p/s in order to make the boundary visible. In fact, this is much larger than the value previously determined, i.e. $I_{\text{crit}} = 1.5 \cdot 10^8$ p/s [13].

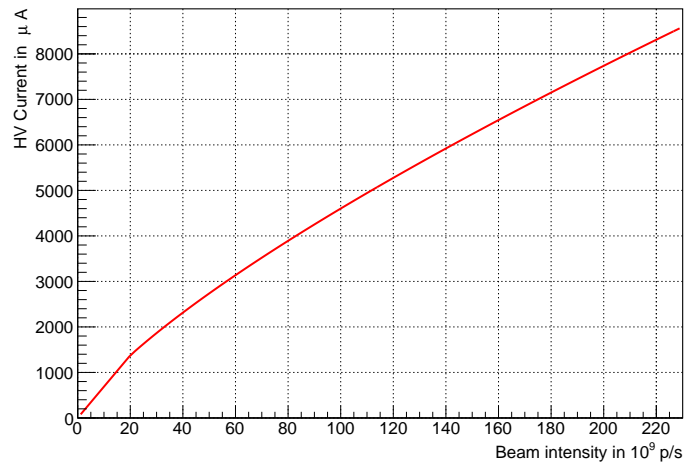


Figure 3.8: Example of the fit model.

Chi-squared fit

4.1 Theory on Chi-squared test

A sensible way of fitting the Hilum data is the so called method of least squares [16]. Assuming a data set of accurately known values x_i and corresponding values y_i with uncertainties σ_i , one has to set up a fit function $f(x_i; a_i)$ with N parameters a_i . Without further proof, the following sum, termed χ^2 , gives a reasonable way of testing the goodness of fit:

$$\chi^2 = \sum_{i=1}^N \left[\frac{y_i - f(x_i; a_i)}{\sigma_i} \right]^2. \quad (4.1)$$

In order to obtain an adequate fit, the parameter set a_i has to be varied until the sum hits a minimum. Moreover, for a valid model one would expect the numerator in eq. (4.1) on average to be about the size of the measurement uncertainty σ_i and hence a contribution from each term equal to one. Thus χ^2 divided by the degrees of freedom (dof), i.e. the total number of data points N minus the amount of parameters a_i used, should yield approximately one¹⁰.

Uncertainties of the x_i are taken into account by converting them into uncertainties for the y_i . This is done by multiplying each x_i uncertainty value with the derivative of the fit function at the considered point. The final χ^2 -function is given by eq. (4.2):

$$\chi^2 = \sum_{i=1}^N \frac{[y_i - f(x_i; a_i)]^2}{\left(\sigma_{x_i} \cdot \frac{\partial f(x_i; a_i)}{\partial x_i} \right)^2 + \sigma_{y_i}^2}. \quad (4.2)$$

4.2 Estimating the unknown systematics

The following chapter explains how the missing systematics as described in section 3.1.2 were estimated. The complete EMEC data sample was split into three parts:

Section 4.2.1 discusses the HV current for beam intensities up to $0.03 \cdot 10^9$ p/s, i.e. a regime that lies well below the expected value of I_{crit} . Then in section 4.2.2 results from linear fits for beam intensities between $0.03 \cdot 10^9$ p/s and $0.2 \cdot 10^9$ p/s are presented. They were conducted

¹⁰The sum given by eq. (4.1) follows a χ^2 probability distribution with $N - n$ degrees of freedom, proof of which can be found in [16]. Strictly speaking, this only holds if the dependency of f on the a_i is linear, which is not true for the parameters p and I_{crit} of the HV current model (see 3.3.2). However, for N large enough the χ^2 -distribution again becomes a valid assumption.

in order to propagate a corresponding slope error, which will be explained in detail. For values above $0.2 \cdot 10^9$ p/s, the HV current was binned. The uncertainties of the beam intensity remain unmodified throughout.

4.2.1 HV current for very low intensities

The HV current for beam intensities below $0.03 \cdot 10^9$ p/s is given by Fig. 4.1. Up to $0.01 \cdot 10^9$ p/s lie six runs, numbered 1102, 1109, 1110, 1111, 1112 and 1117. Between $0.01 \cdot 10^9$ p/s and $0.025 \cdot 10^9$ p/s there is a single run (number 1099). The HV current uncertainties were left unaltered in this regime.

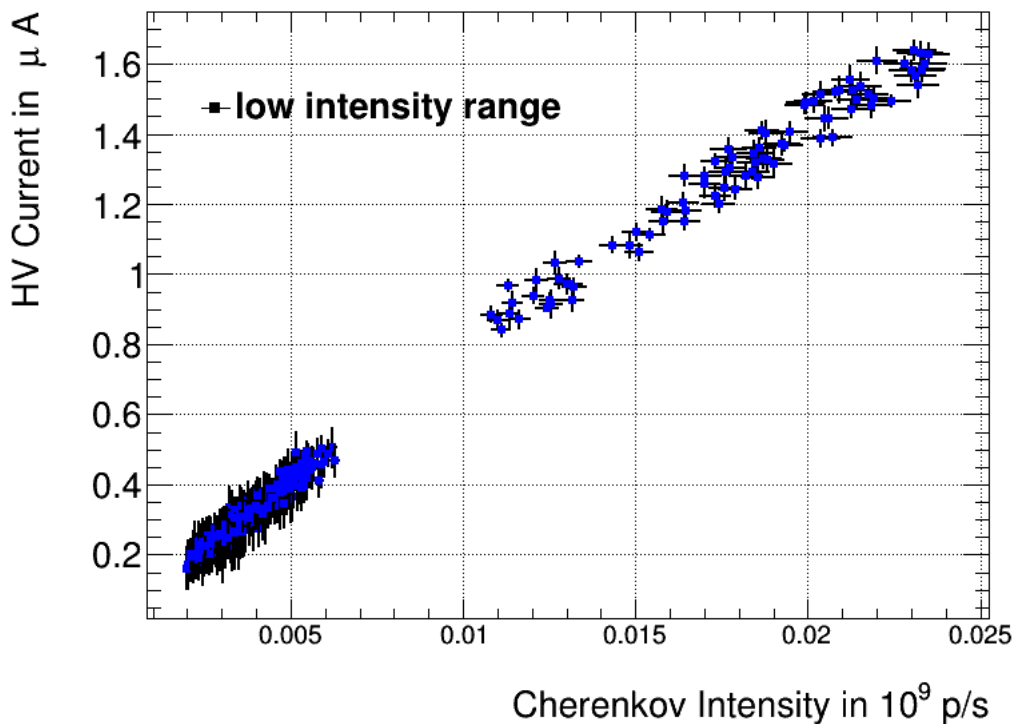


Figure 4.1: HV current for beam intensities below $0.03 \cdot 10^9$ p/s.

4.2.2 Linear fits within low intensity range

In Fig. 4.2 run number 1098 is depicted in addition to the six runs listed in section 4.2.1. Each run was fitted linearly. The outcome can be seen in Tab. 4.1. The two slope values furthest apart amount to $m_{\min} = 62.1 \mu\text{A per } 10^9 \text{ p/s}$ and $m_{\max} = 81.1 \mu\text{A per } 10^9 \text{ p/s}$ and belong to run 1099 and run 1098 respectively. The absolute difference between the corresponding fit functions (also drawn in Fig. 4.2) was calculated and a new uncertainty $\Delta I_{\text{HV, slope}}$ added to the existing one:

$$\Delta I_{\text{HV, slope}}(I) = | I_{\min} + m_{\min} \cdot I_{\text{HV}}(I) - (I_{\max} + m_{\max} \cdot I_{\text{HV}}(I)) |. \quad (4.3)$$

This was done for beam intensities between $0.03 \cdot 10^9$ p/s and $0.2 \cdot 10^9$ p/s. Please note that I_{\min} and I_{\max} do not denote the lowest and highest offset values obtained from the linear fits, but the results that correspond with m_{\min} and m_{\max} .

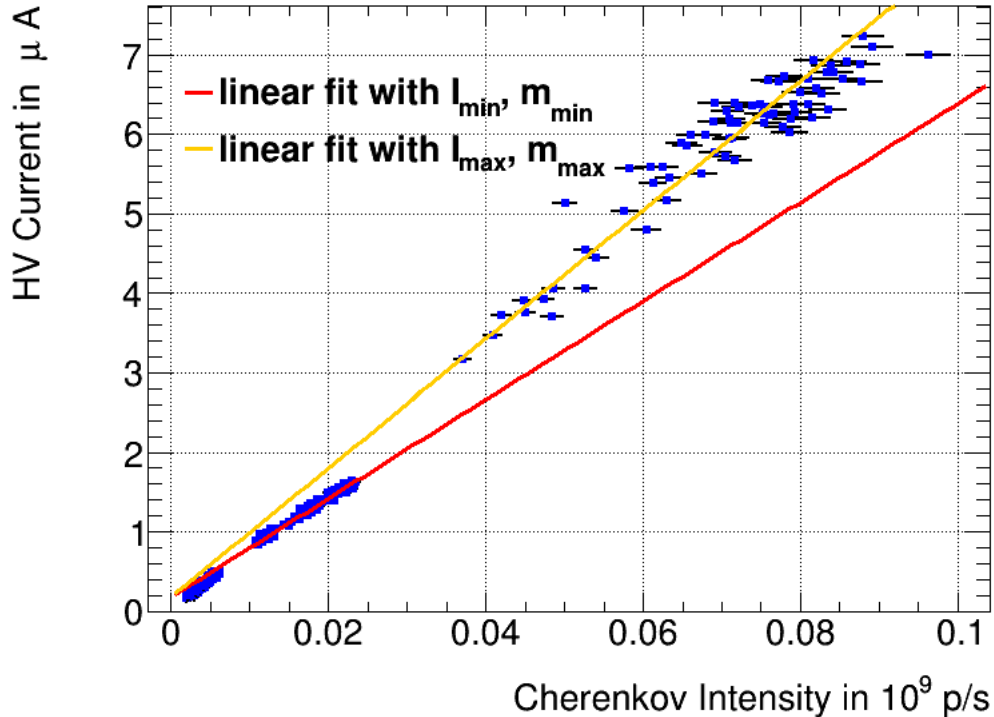


Figure 4.2: Linear fits with minimal and maximal slope for runs 1098, 1099, 1102, 1109, 1110, 1111, 1112 and 1117.

Table 4.1: Fit results for the linearly fitted low intensity runs.

run number	I_0 in μA	m in μA per 10^9 p/s
1098	0.183	81.1
1099	0.179	62.1
1102	0.0561	68.3
1109	0.0274	73.7
1110	0.0144	78.5
1111	0.0475	72.5
1112	0.0404	75.4
1117	0.0399	75.6

4.2.3 HV current binning

To account for the unknown systematics above $0.2 \cdot 10^9$ p/s, the HV current was binned. The according bins for beam intensities between $2 \cdot 10^9$ p/s and $220 \cdot 10^9$ p/s are shown in Fig. 4.3, those for values below $1 \cdot 10^9$ in Fig. 4.4. The bin with limits $1 \cdot 10^9$ and $2 \cdot 10^9$ is spread

between the two diagrams. The red area in Fig. 4.4 indicates where the slope uncertainty has been propagated (see section 4.2.2). For a detailed list of the bin limits see appendix A.3.

For each bin a new uncertainty $\Delta I_{\text{HV,bin}}$ was worked out:

$$\Delta I_{\text{HV, bin}} = \sqrt{\sigma_{\text{bin}}^2 + \Delta I_{\text{HV, existing}}^2}, \quad (4.4)$$

where $\Delta I_{\text{HV, existing}}$ denotes the original HV current uncertainty and σ_{bin} the standard deviation of the HV current.

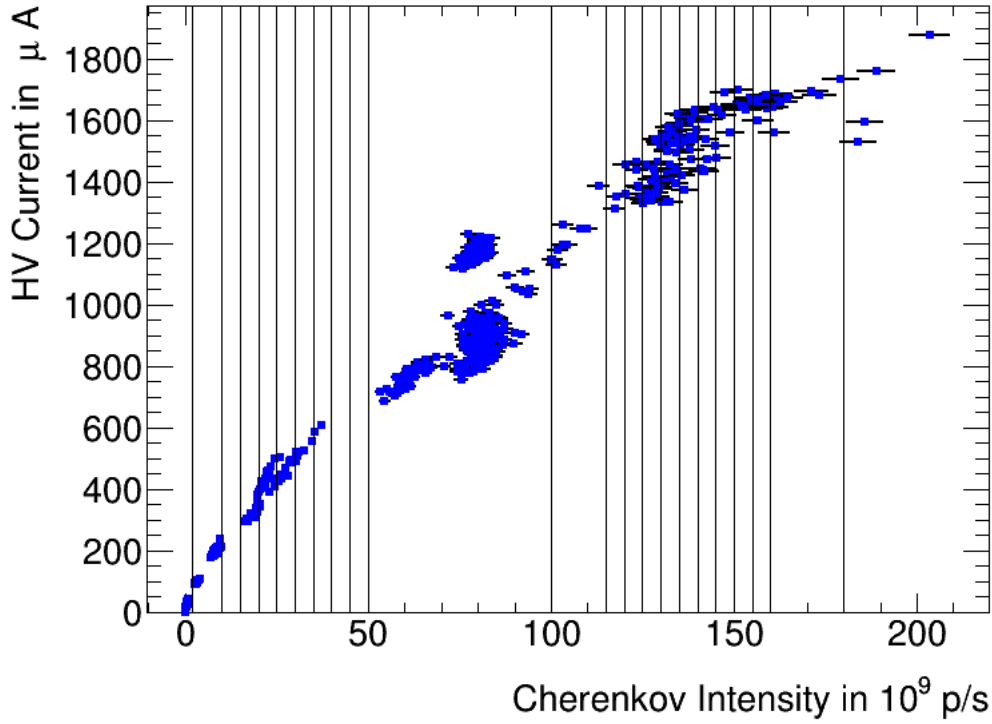


Figure 4.3: HV current bins for intensities between $2 \cdot 10^9$ p/s and $220 \cdot 10^9$ p/s.

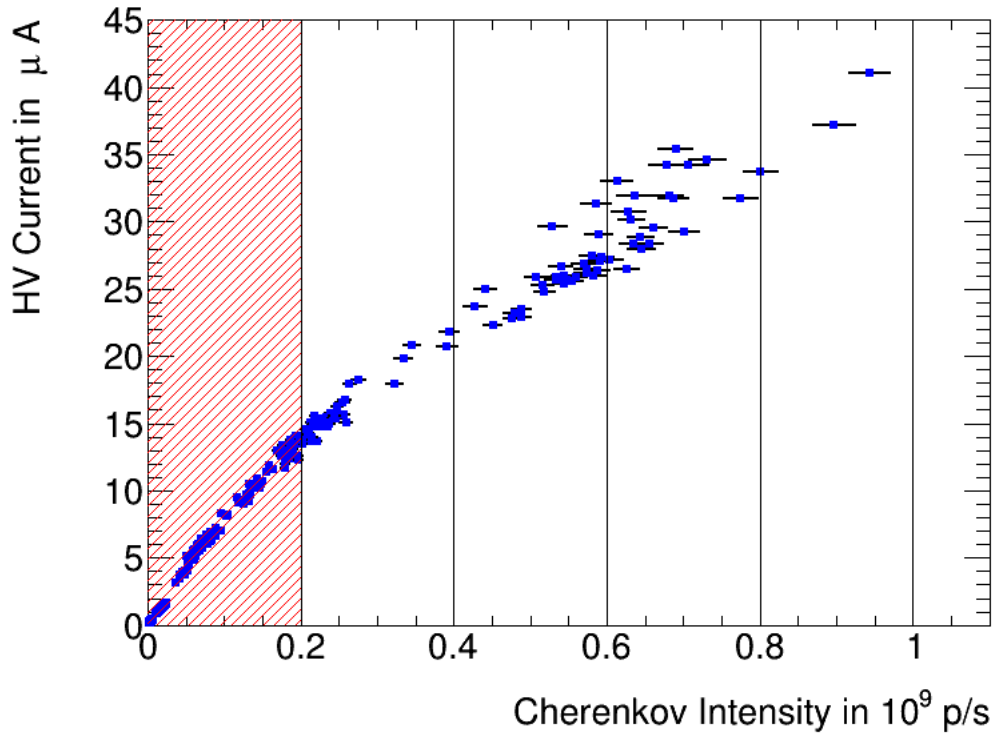


Figure 4.4: HV current bins for intensities below $1 \cdot 10^9$ p/s.

4.3 Fit results

The final fit can be seen in Fig. 4.5 and the corresponding parameter values are listed in Tab. 4.2. The results were obtained by applying the uncertainty scaling methods described in sections 4.2.1 through 4.2.3. Ultimately, a χ^2/dof of 1.0293 was achieved.

The uncertainties stated in Tab. 4.2 refer to a confidence level of 68.3% and were obtained by evaluating the parameter space that belongs to a χ^2 value raised by $\Delta\chi^2 = 4.7$ above the minimal χ^2 value¹¹. This leads to asymmetric uncertainties, which were found to be symmetric within the quoted significance range and are therefore not stated.

I_{crit} was found to be $(0.114 \pm 0.005) \cdot 10^9$ p/s with a relative uncertainty of 4.4%. The fit function and HV current for the corresponding range of the beam intensity are depicted in Fig.4.6. In addition, its uncertainty has been calculated by setting m , I_0 and p to their final values as in Tab. 4.2, minimizing the χ^2 -function for the one-dimensional subspace of I_{crit} and determining the value of I_{crit} for a $\Delta\chi^2$ of 1¹². This leads to a refined uncertainty of $0.003 \cdot 10^9$ p/s (2.6%) with a confidence level of 68.3%.

The parameters I_0 , m , I_{crit} and p are correlated with their correlation coefficients given in

¹¹the parameter set of a χ^2 -fit follows a χ^2 probability distribution; for a recipe of how the uncertainties on parameters that result from a χ^2 fit are to be determined, please see appendix A.4

¹²for a correct profiling procedure, the nuisance parameters m , I_0 and p need to be minimized for every value of I_{crit}

Tab. 4.3¹³. Note that there are parameters that are highly correlated, e.g. I_0 and m with a correlation coefficient of -0.8189, and some that are almost independent of each other (I_0 , p and m , p).

Table 4.2: Final fit results.

parameter	value
I_0	$(0.071 \pm 0.008) \mu\text{A}$
m	$(67.9 \pm 0.6) \mu\text{A per } 10^9 \text{ p/s}$
I_{crit}	$(0.114 \pm 0.005) \cdot 10^9 \text{ p/s}$
p	0.741 ± 0.002

Table 4.3: Correlation coefficients for I_0 , m , I_{crit} and p .

parameter combination	correlation coefficient
I_0, m	-0.8189
I_0, I_{crit}	0.5986
I_0, p	0.0136
m, I_{crit}	-0.7351
m, p	-0.0122
I_{crit}, p	-0.6675

¹³consider the χ^2 -distribution of the parameters and appendix A.5

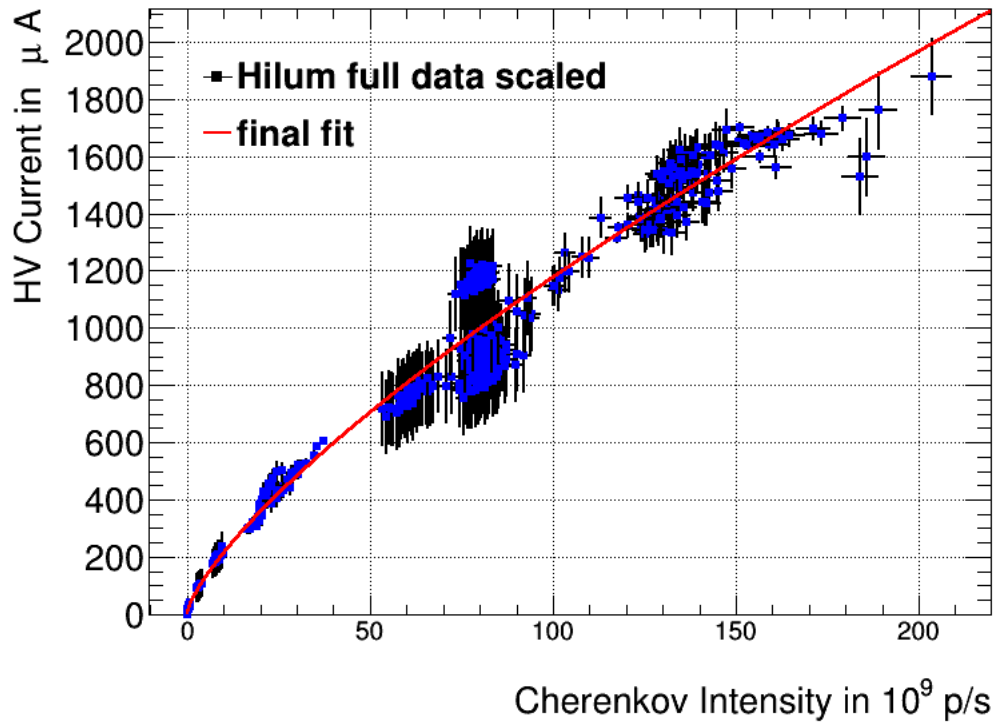


Figure 4.5: Hilum data with modified HV current uncertainties and final fit.

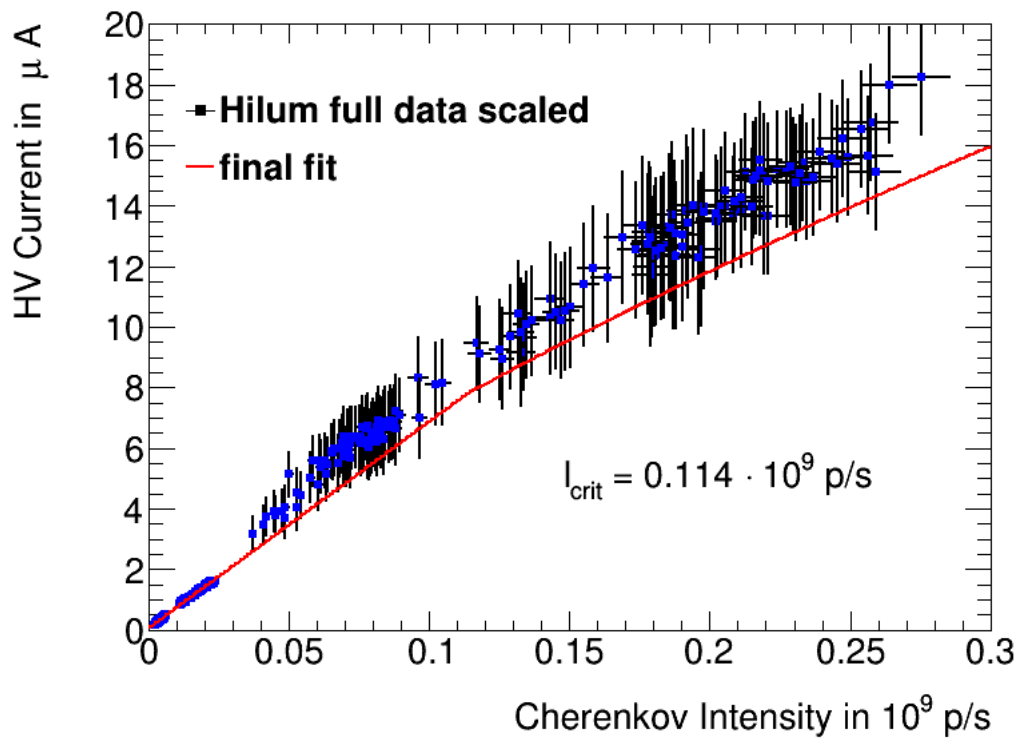


Figure 4.6: Final fit with scaled HV current uncertainties for beam intensities near I_{crit} .

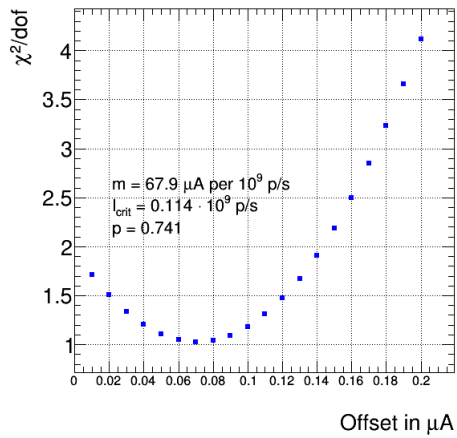
4.4 Fit stability

The stability of the fit was tested by setting three out of four parameters to their final fit values as stated in section 4.3 and scanning through the remaining one. Fig. 4.7a through Fig. 4.7d depict the corresponding χ^2/dof graphs, where the degrees of freedom now count 1230. Apparently, the scanning ranges are fairly narrow and hence one may not conclude that the overall fit is stable from the given figures alone. Therefore all four parameters were roughly scanned within the reasonably largest interval, i.e. 0 μA to 2000 μA for the offset, 0 μA per 10^9 p/s to 200 μA per 10^9 p/s for the slope, 0 to $200 \cdot 10^9$ p/s for the critical intensity and 0 to 2 for the exponent. Leaving the regimes given by Fig. 4.7 quickly lead to χ^2 values of several millions and no further minima were detected. Evidently, the quadratic behaviour shows a fit that settles well into the final parameter values. However, this test could be refined a lot by varying two or even three rather than just one parameter at a time. In this case further minima might occur.

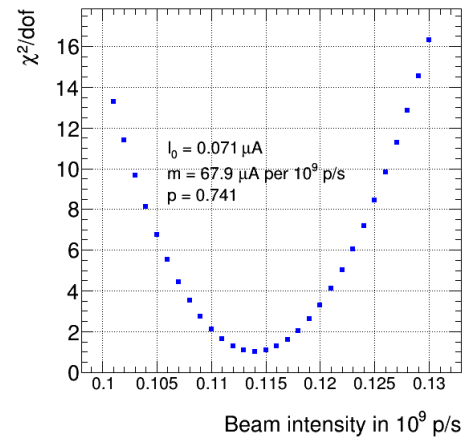
An example of what a two parameter variation might look like can be seen in Fig. 4.8. Altering the offset or the slope (or both at the same time) did not seem a good idea, since then the fit function would quickly miss the linear low intensity regime. Therefore, the only combination that seemed promising, the critical intensity and the power, were altered. Most remarkably, there indeed exists a rather wide valley in which the χ^2/dof does not change very much, as demonstrated in Tab. 4.4.

Table 4.4: χ^2/dof values for several points within the valley structure.

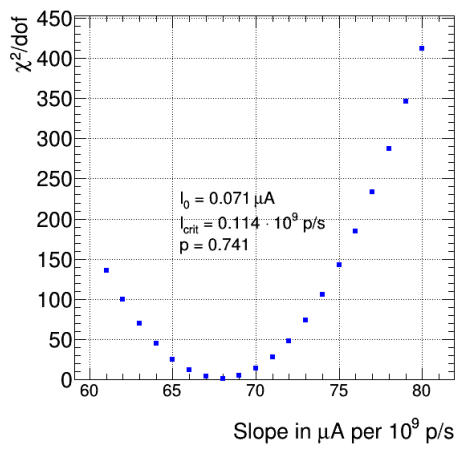
I_{crit} in 10^9 p/s	p	χ^2/dof
0.04	0.80	5.5523
0.08	0.76	1.4513
0.12	0.74	1.6448
0.16	0.72	1.5497
0.20	0.70	6.7919



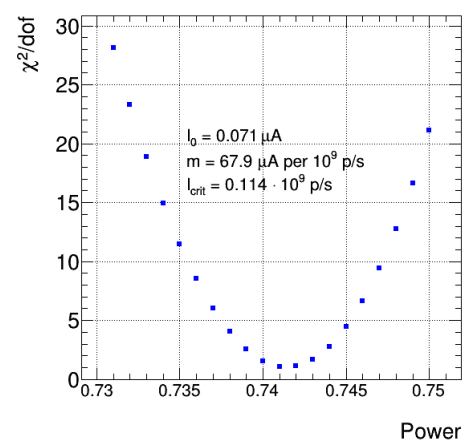
(a) Offset scan.



(b) Critical intensity scan.



(c) Slope scan.



(d) Power scan.

Figure 4.7: χ^2/dof scan for every parameter. The remaining parameters are set to their final values.

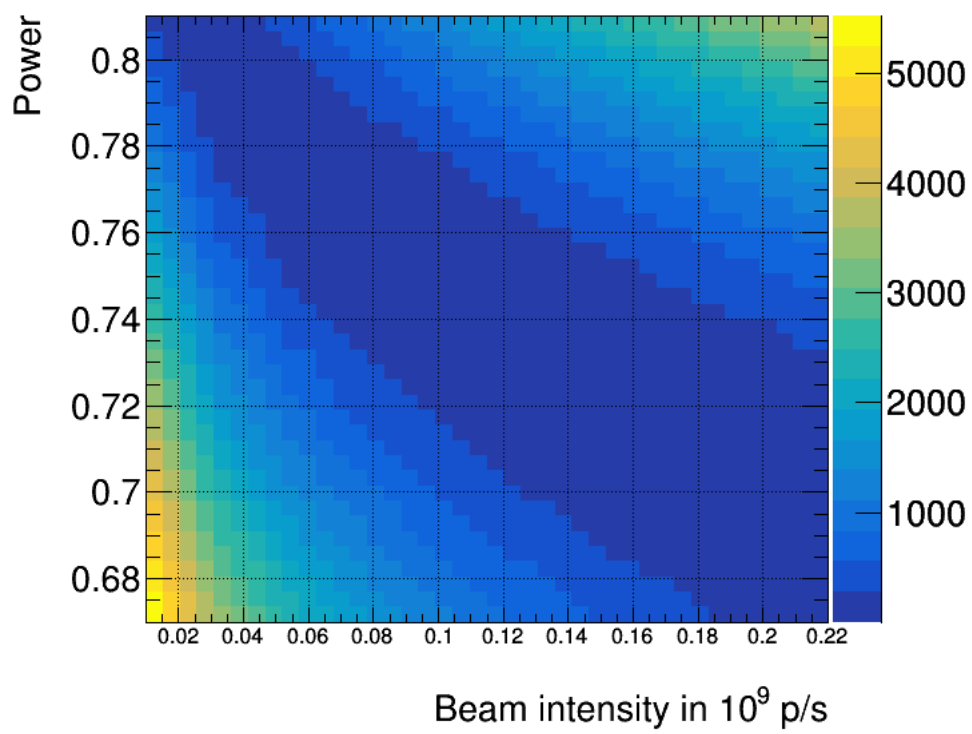


Figure 4.8: χ^2/dof for intensity and power scanning.

Summary and Outlook

In sections 3.1 and 3.2 the EMEC data set with its existing uncertainties was introduced. As explained in section 3.1.2, the uncertainties did not account for the large fluctuations of the HV current. In order to obtain I_{crit} according to the fit model described in 3.3.2, the unknown systematics had to be estimated. The χ^2 fitting procedure consisted of three parts: a low intensity regime for which the uncertainties remained unscaled (section 4.2.1), linear fits for some data taking periods that led to a propagated slope uncertainty (section 4.2.2) and the introduction of HV current bins (section 4.2.3).

The fit yielded a value for I_{crit} of $(0.114 \pm 0.005) \cdot 10^9$ p/s (4.4%) and $(0.114 \pm 0.003) \cdot 10^9$ p/s (2.6%) with respect to the two different methods of obtaining confidence intervals for multi-parameter fits mentioned in 4.3. In section 4.4 the stability of the fit was tested by scanning through one parameter at a time. Previously, I_{crit} has been evaluated to $1.5 \cdot 10^8$ p/s with a relative systematic uncertainty of 50% [13]. Thus the uncertainty on I_{crit} could be improved. However, estimating the systematic uncertainties from the data is rather unsatisfactory. Preferably, the data set should account for any systematics by itself, making the subsequent modification of the uncertainties redundant. Considering the future of Hilum, the experiment has to be improved to eliminate the error sources discussed in section 3.1.2.

Beyond the extent of this thesis, the data calculated via the integral method and the additional amplitude two and three sample files (as explained in section 3.2.1) may be analysed using an approach similar to the one presented here. Perhaps a more precise I_{crit} would be achieved this way, either by comparing the outcome regarding the different current measuring methods or by selecting the one to be known most accurate.

Appendix

A.1 Average HV current per data taking period

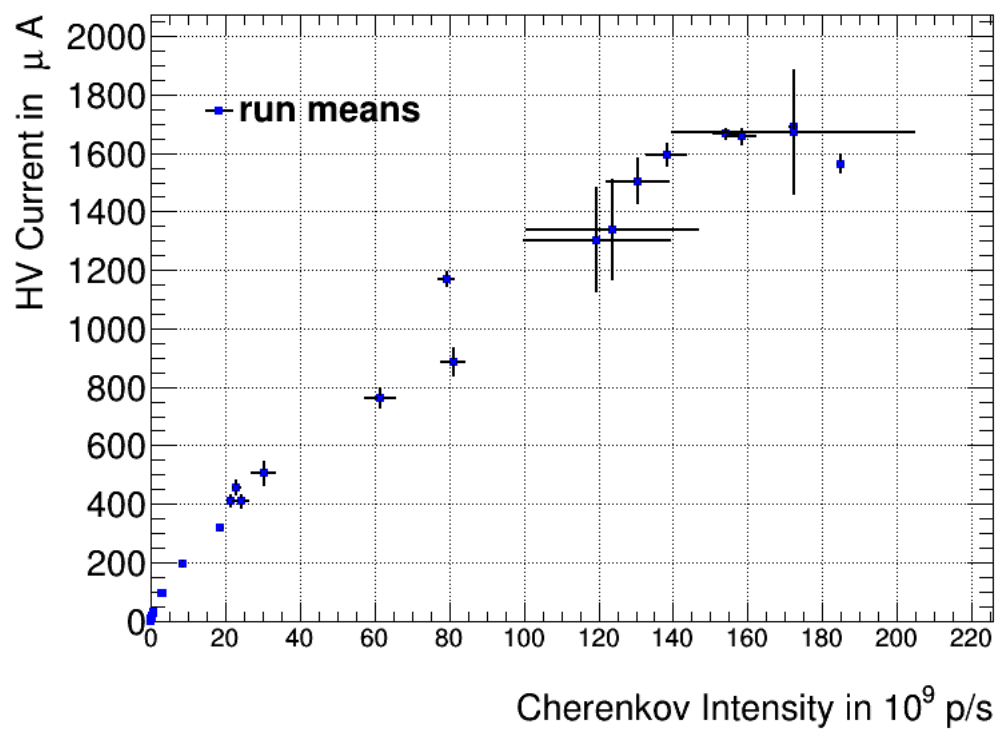


Figure A.1: Run-wise means with the standard deviation taken as uncertainties on the beam intensity and the HV current.

A.2 List of data taking periods

Table A.1: List of every run with corresponding correlation coefficient ρ and the ranges of the beam intensity and HV current.

run number	ρ	beam intensity range in 10^9 p/s	HV current range in μA
1074	0.960255	24.0106-37.4539	433.038-606.062
1080	0.93986	19.8547-26.5053	358.312-434.194
1083	0.820402	6.82539-10.0119	176.04-238.607
1084	0.727196	2.73872-3.26149	88.9708-99.1637
1085	0.954565	2.69066-4.09351	89.4786-107.453
1087	0.967629	0.450986-0.943692	22.2679-41.0402
1089	0.979249	0.0958705-0.42789	8.33224-23.6868
1090	0.965746	0.394585-0.731484	21.8208-35.3846
1092	0.957933	0.0865248-0.259059	6.77798-15.6635
1093	0.984396	0.102125-0.243486	8.11051-15.5633
1098	0.949482	0.037068-0.0963192	3.16674-7.23776
1099	0.983296	0.0108247-0.0234996	0.840942-1.63814
1102	0.935738	0.00222445-0.00619218	0.177226-0.505487
1109	0.889153	0.00231078-0.00500096	0.190804-0.391065
1110	0.943904	0.00220129-0.00546302	0.179931-0.44264
1111	0.969517	0.00199369-0.00547633	0.16166-0.461587
1112	0.953996	0.002092-0.00535374	0.190265-0.439687
1117	0.932959	0.0025266-0.00627526	0.224965-0.502659
1130	0.858423	53.2163-72.4412	687.571-830.926
1131	0.874559	16.6142-20.5682	295.445-351.041
1141	0.971308	19.9004-23.0582	381.328-456.381
1142	0.948644	20.9941-25.8803	415.467-503.932
1165	0.583706	73.2998-83.68	1114.3-1227.53
1169	0.457008	74.4582-101.518	753.651-1130.7
1170	1	183.985-185.83	1529.05-1596.68
1172	-1	171.051-173.479	1680.17-1697.13
1175	0.0822588	150.682-164.494	1559.78-1686.11
1176	0.980919	65.6826-141.728	822.537-1504.69
1180	0.844917	123.546-146.621	1463.1-1641.19
1181	0.882058	103.39-143.201	1261.06-1620.31
1182	-0.39749	147.531-158.998	1640.14-1700.16
1183	0.998245	117.359-203.488	1313.68-1878.18
1184	0.990629	71.7989-160.472	963.647-1641.6

A.3 Widths of HV current bins.

Table A.2: Widths of HV current bins.

bin number	1	2	3	4	5	6	7	8
bin limits in 10^9 p/s	0.2-0.4	0.4-0.6	0.6-0.8	0.8-1.0	1.0-2.0	2.0-10	10-15	15-20
9	10	11	12	13	14	15	16	17
20-25	25-30	30-35	35-40	40-45	45-50	50-100	100-115	115-120
120-125	125-130	130-135	135-140	140-145	145-150	150-155	155-160	160-180
180-220	180-220	180-220	180-220	180-220	180-220	180-220	180-220	180-220

A.4 Estimating the uncertainty intervals for multi-parameter chi-squared fits

The following merely provides a recipe for estimating the confidence intervals of a multi-parameter χ^2 -fit [17].

For a χ^2 -test that uses a fit function f with n parameters a_i , a χ^2 -distribution is given by

$$\chi^2 = \sum_{i=1}^n \left[\frac{\hat{a}_i - f(a_i; x_i)}{\sigma_{a_i}} \right]^2, \quad (\text{A.1})$$

where \hat{a}_i denotes the estimate of the parameter a_i (obtained from the χ^2 -test performed on the data set), σ_{a_i} the uncertainty on \hat{a}_i and the x_i the (fixed) values from the observation.

Assuming that the confidence intervals for a subset of k parameters taken from the a_i are to be evaluated, the following instruction has to be followed:

First, the cumulative distribution function (cdf) for a χ^2 -distribution with k degrees of freedom is looked up (see Fig. A.2). Then the function value of the cdf is set to the probability content β . Evaluating the corresponding argument defines a $\Delta\chi^2$ value. The χ^2 -distribution as in eq. (A.1) has to be minimized with respect to all the uninteresting parameters for every point in the k -dimensional subspace of the interesting ones. Then the χ^2 value is incremented by $\Delta\chi^2$ and the confidence intervals obtained from the corresponding confidence region.

The statement that can be made is that the k parameters from the subset of the a_i lie within the obtained confidence intervals with probability β , whatever the values of the remaining parameters. Tab. A.3 shows several $\Delta\chi^2$ values with respect to β and k , in particular those used in section 4.3, i.e. $\Delta\chi^2 = 4.72$ for 4 parameters and $\Delta\chi^2 = 1$ for a single parameter with $\beta = 68.3\%$ in both cases.

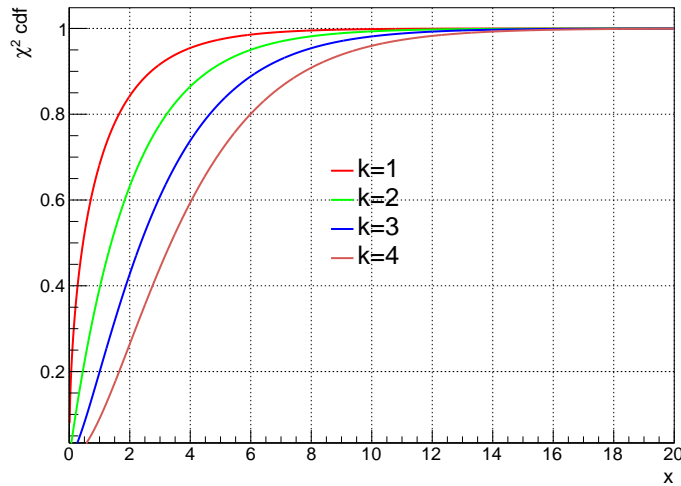


Figure A.2: Cumulative distribution function (cdf) for a χ^2 probability distribution and k degrees of freedom.

Table A.3: $\Delta\chi^2$ values for specified probability content β and k parameters.

β	$k = 1$	$k = 2$	$k = 3$	$k = 4$
68.3%	1.00	2.30	3.53	4.72
95.5%	4.02	6.20	8.05	9.74
99.7%	8.81	11.6	13.9	16.0

A.5 Theory on correlation

For a data sample with items x_i , each with uncertainty σ_{x_i} and a pairwise correlation coefficient ρ_{ij} for items i and j , we obtain a rather convenient way of writing down the χ^2 -function:

$$\chi^2 = \begin{pmatrix} y_1 - f(x_1; a_i) \\ y_2 - f(x_2; a_i) \\ \vdots \\ y_N - f(x_N; a_i) \end{pmatrix}^T V^{-1} \begin{pmatrix} y_1 - f(x_1; a_i) \\ y_2 - f(x_2; a_i) \\ \vdots \\ y_N - f(x_N; a_i) \end{pmatrix}, \quad (\text{A.2})$$

where V^{-1} denotes the inverse of the covariance matrix

$$V = \begin{pmatrix} \sigma_1\sigma_1 & \rho_{12}\sigma_1\sigma_2 & \rho_{13}\sigma_1\sigma_3 & \dots \\ \rho_{12}\sigma_1\sigma_2 & \sigma_2\sigma_2 & \rho_{23}\sigma_2\sigma_3 & \dots \\ \rho_{13}\sigma_1\sigma_3 & \rho_{23}\sigma_2\sigma_3 & \ddots & \\ \vdots & \vdots & & \end{pmatrix}. \quad (\text{A.3})$$

Please note that V is obviously symmetrical.

In the case of no correlation, i.e. $\rho_{ij} = 0$, the matrix V becomes diagonal with entries σ_i^2 , simply being the variance of the x_i . Calculating V^{-1} then becomes very easy, as one only has

to work out the reciprocal variance values:

$$V^{-1} = \begin{pmatrix} \sigma_1^{-2} & \dots & & \\ \vdots & \sigma_2^{-2} & & \\ & & \ddots & \\ & & & \ddots \end{pmatrix}. \quad (\text{A.4})$$

A.6 Hilum data correlation

To include possible correlation-based relations within the data set, the covariance matrix (see eq. (A.3)) was calculated as follows. Each entry was set to

$$V_{ij} = \sum_{k=1}^4 \rho_k \cdot \Delta I_k^i \cdot \Delta I_k^j, \quad (\text{A.5})$$

where the indices i and j refer to the individual runs. The ΔI_k were obtained by calculating the run-wise standard deviation of the HV current¹⁴

$$\Delta I_1 = I_{\text{RMS}}^{\text{HV}}, \quad (\text{A.6})$$

the propagated standard deviation of the run intensity

$$\Delta I_2 = I_{\text{RMS}} \cdot \frac{\partial I_{\text{HV}}}{\partial I}(I = I_{\text{mean}}), \quad (\text{A.7})$$

the averaged original uncertainties of the HV current

$$\Delta I_3 = \frac{\sqrt{\sum_{l=1}^n \Delta I_{l,\text{HV}}^2}}{n}, \quad (\text{A.8})$$

and the averaged propagated original uncertainties of the intensity

$$\Delta I_4 = \frac{\sqrt{\sum_{l=1}^n (\Delta I_l \cdot \frac{\partial I_{\text{HV}}}{\partial I}(I = I_l))^2}}{n}, \quad (\text{A.9})$$

Here n denotes the total amount of points per run and l is the run-wise summation index. For reasons of simplicity the ρ_k were assumed to be constant, though they may also be given a dependency of i and j .

¹⁴the abbreviation RMS is used as a synonym for standard deviation

Bibliography

- [1] Lyndon Evans and Philip Bryant. “LHC Machine”. In: *Journal of Instrumentation* 3.08 (2008), S08001. URL: <http://stacks.iop.org/1748-0221/3/i=08/a=S08001>.
- [2] P. La Rocca and F. Riggi. “The upgrade programme of the major experiments at the Large Hadron Collider”. In: *Journal of Physics: Conference Series* 515 (2014).
- [3] “The ATLAS Experiment at the CERN Large Hadron Collider”. In: *JINST* 3 (2008), S08003. DOI: 10.1088/1748-0221/3/08/S08003.
- [4] *ATLAS Phase-II Upgrade Scoping Document*. Tech. rep. CERN-LHCC-2015-020. LHCC-G-166. Geneva: CERN, 2015. URL: <https://cds.cern.ch/record/2055248>.
- [5] Collaboration ATLAS. *Letter of Intent for the Phase-II Upgrade of the ATLAS Experiment*. Tech. rep. CERN-LHCC-2012-022. LHCC-I-023. Draft version for comments. Geneva: CERN, 2012. URL: <https://cds.cern.ch/record/1502664>.
- [6] Peter Krieger. “ATLAS Calorimetry at the Large Hadron Collider”. WRNPPC. 2004.
- [7] Frank Seifert. “Relative Luminosity Measurement of the LHC with ATLAS FCAL HV currents”. Diplomarbeit. TU Dresden, 2008.
- [8] *An instrumentation drawer of the barrel tile calorimeter of the ATLAS experiment*. Aug. 16, 2016. URL: <https://cds.cern.ch/record/1696890>.
- [9] CERN Document Server. *The ATLAS electromagnetic calorimeter*. Aug. 16, 2016. URL: <https://cds.cern.ch/record/636674#03>.
- [10] S. Ivanov. “Accelerator complex U70 of IHEP: Present status and recent upgrades”. In: *Proceedings RuPAC-2010* (2010), pp. 30–31.
- [11] Peter Schacht. “Hilum Status June 2016”. LAr Endcap Hilum Meeting. 2016.
- [12] Olga Novgorodova. “ATLAS LAr Calorimeter Degradation Studies for HL-LHC”. Tagung DPG Wuppertal. 2015.
- [13] A. Glatte et al. “Liquid argon calorimeter performance at high rates”. In: *Nuclear Instruments and Methods in Physics Research A* 669 (2012).
- [14] Frank Seifert. “ $Z \rightarrow \tau\tau$ Cross Section Measurement and Liquid-Argon Calorimeter Performance at High Rates at the ATLAS Experiment”. PhD thesis. TU Dresden, 2012.

- [15] John P. Rutherford. “Signal degradation due to charge buildup in noble liquid ionization calorimeters”. In: *Nuclear Instruments and Methods in Physics Research A* 482 (2002) 156–178 (2002).
- [16] R. J. Barlow. *Statistics - A guide to the Use of Statistical Methods in the Physical Sciences*. John Wiley and Sons.
- [17] Yoram Avni. “Energy Spectra of X-Ray Clusters of Galaxies”. In: *The Astrophysical Journal* 210:642-646 (1976).

Erklärung

Hiermit erkläre ich, dass ich diese Arbeit im Rahmen der Betreuung am Institut für Kern- und Teilchenphysik ohne unzulässige Hilfe Dritter verfasst und alle Quellen als solche gekennzeichnet habe.

Fabian Petsch

Dresden, September 2016